bioRxiv preprint doi: https://doi.org/10.1101/232066; this version posted December 10, 2017. The copyright holder for this preprint (which was not certified by peer review) is the author/funder, who has granted bioRxiv a license to display the preprint in perpetuity. It is made available under aCC-BY-NC-ND 4.0 International license.

Decoupling cellular response to topography and stiffness in three dimensions

Colin D. Paul, Alex Hruska, Jack R. Staunton, Hannah A. Burr, Jiyun Kim, Nancy Jiang, and Kandice Tanner*

[a]Laboratory of Cell Biology, Center for Cancer Research, National Cancer Institute, National Institutes of Health

* Corresponding author information: Dr. Kandice Tanner; Center for Cancer Research, National Cancer Institute, Building 37, Room 2132, Bethesda, MD 20892; Ph: 260-760-6882; Email: kandice.tanner@nih.gov

bioRxiv preprint doi: https://doi.org/10.1101/232066; this version posted December 10, 2017. The copyright holder for this preprint (which was not certified by peer review) is the author/funder, who has granted bioRxiv a license to display the preprint in perpetuity. It is made available under aCC-BY-NC-ND 4.0 International license.

ABSTRACT

Biophysical aspects of in vivo tissue microenvironments include microscale mechanical properties, fibrillar alignment, architecture or topography of the extracellular matrix (ECM), and the repertoire of ECM ligands present, all of which provide cues to drive cellular response. Cell-ECM interactions are important regulators of both normal tissue homeostasis and malignancy. Thus, understanding both extracellular cues and the cellular responses they elicit is fundamental to developing therapeutic strategies. Various in vitro platforms for 3D cell culture and tissue engineering have been used to study cellular response to the microenvironment. However, recapitulating the diversity of tissue architectures present in vivo in a controlled manner in three-dimensional tissue mimetics is challenging using naturally derived ECM hydrogels. Here, we use a bottom-up approach to build fibrillar architecture into 3D amorphous hydrogels using self-assembly of magnetic colloidal particles functionalized with human ECM proteins. Human ECM proteins associated with organ-specific pathological states were used. We determined that, while the bulk tissue mechanics of hydrogels containing either aligned fibers or randomly distributed colloidal particles were similar, aligned hydrogels exhibited spatial heterogeneities in microscale mechanical properties near aligned fibers. We then used this platform in combination with 2D substrates of defined elastic modulus to decouple the role of topography from microscale tissue mechanics for normal and tumor cells. We determined that topographical cues dominate cellular response for human and normal cells, which responded independently of microscale mechanics and ECM composition in 3D hydrogels. These data suggest that topography alone can drive fundamental cellular responses such as polarization and migration for both normal and transformed cells.

bioRxiv preprint doi: https://doi.org/10.1101/232066; this version posted December 10, 2017. The copyright holder for this preprint (which was not certified by peer review) is the author/funder, who has granted bioRxiv a license to display the preprint in perpetuity. It is made available under aCC-BY-NC-ND 4.0 International license.

INTRODUCTION

The physical properties of the extracellular matrix (ECM) milieu are becoming more widely acknowledged as fundamental determinants of cell fate, tissue homeostasis, immune response, wound healing, and cancer progression(1-4). Within a given tissue, the ECM not only provides structural support but regulates cell signaling via reciprocal biochemical and biophysical cues(5). On one hand, the ECM contributes to overall tissue mechanics, and the effects of mechanical properties on cell fate and phenotype have been extensively studied using in vitro and in vivo assays(6-15). For example, tissues become progressively stiffer as a function of malignant transformation from normal to tumors(9). In addition, the architecture of the ECM provides structural feedback, such as topographical cues(13-16). Topography, simply described, refers to the shape and profile of a given material's surface(17-19). In vivo, tissue contains hybrid structures comprised of aligned ridges and pores that span lengths from nanoscale to microscale(17-19). On the nanoscale level, ECM proteins can adopt different morphologies, such as globular and fibrillar architectures(17, 18). One such example is fibronectin (FN), which presents different cell binding sites and is alternatively spliced to generate conformation which initiate distinct signaling cascades(20, 21). Based on microscale tissue architecture, cells can execute different modes of motility and tissue remodeling (22-25). For example, in the MMTV-PyVT murine model for mammary cancer, tumor cells preferentially migrate along aligned collagen fibers oriented radially to the primary tumor as opposed to circumferential fibers wrapping around the tumor boundary(14). Similar observations have been deduced using in vitro models, where breast cancer cells show increased individual cell displacement along aligned fibers without changing overall cell speed in 3D collagen hydrogels(26). Topographical cues also play a role in distal organ colonization during metastasis. Vascular co-option is one strategy used by tumor cells to access nutrients in order to proliferate at distant sites(27, 28). In cases of metastasis to the brain, breast,

bioRxiv preprint doi: https://doi.org/10.1101/232066; this version posted December 10, 2017. The copyright holder for this preprint (which was not certified by peer review) is the author/funder, who has granted bioRxiv a license to display the preprint in perpetuity. It is made available under aCC-BY-NC-ND 4.0 International license.

melanoma and lung cancer cells have been found to interact with the undulating basement membrane along the curvature of the existing blood vessels(27, 28). Glioblastomas have also been found to preferentially migrate and proliferate on brain vasculature using a rodent model and an in vitro model for confined migration (29). Not restricted to in vitro and animal models, these cellular responses are clinically relevant for human patients. The presence of aligned collagen fibers around the periphery of human primary breast tumors is an independent prognostic indicator, with both disease-free and disease-specific survival decreasing for patients with such an ECM signature(30). This architecture is thought to be more permissive for tumor cell dissemination. In a similar vein, gliomas are highly migratory along white matter tracts in the brain (31). In patients, surgical resection is impossible(32). Therefore, understanding how and why cells respond to both topography and stiffness could help generate new therapeutics.

Cells interpret topographical and stiffness mediated cues through biochemical signaling via cellular adhesions and cytoskeletal attachments to the ECM(33). However, technical difficulties in decoupling microenvironmental stiffness and topography in three dimensional environments have made it difficult to elucidate the contributions of each of these factors on cell behavior. Cell mechanosensing is a complex phenomenon where topographical cues via cell-extracellular matrix (ECM) adhesion molecules act concomitantly with intracellular machinery to drive cellular responses (34). While studies using patterned two-dimensional substrates(35, 36) and microfabricated environments(37) have revealed aspects of cell response to topography, reaction to topographic cues in more physiologically relevant three-dimensional environments are not well understood. Importantly, three-dimensional cues are likely vital to recapitulate some aspects of physiological mechanosensing. In tissue, 3D topographies consist of highly oriented structures that are not well-recapitulated by *in vitro* hydrogel models. For example, commonly

bioRxiv preprint doi: https://doi.org/10.1101/232066; this version posted December 10, 2017. The copyright holder for this preprint (which was not certified by peer review) is the author/funder, who has granted bioRxiv a license to display the preprint in perpetuity. It is made available under aCC-BY-NC-ND 4.0 International license.

used collagen hydrogels form with fibers that are randomly oriented unless some external micropatterning is imposed during their polymerization (38). Similarly, laminin rich ECMs (Matrigel) form amorphous gels devoid of cell-scale structures(39). To address the need for reproducible 3D culture systems with well-defined matrix architecture and ECM protein composition, we recently developed a method whereby functionalized paramagnetic nanoparticles are magnetically aligned in 3D hydrogels to create fibrils that span microns in length and 10s of nms in widths(17, 40). Fiber alignment, diameter, spacing, and extracellular matrix conjugation to the nanoparticles can be controlled to create defined topography independently of ligand concentration. In these matrices, mouse fibroblasts and neural cell lines send out protrusions either parallel or perpendicular to fibers in a manner dependent on myosin II-contractility, independently of the chemistry of the ECM ligand or hydrogel employed. In this system, bulk mechanical properties were similar. Here, we humanized our system to discern the role of ECM composition on human cell response to topography. Using this system, we decoupled the role of topographical and micromechanics for human normal and cancer cells. Combined with active microrheology, we used our novel three-dimensional fiber fabrication system to measure the cues that cells receive from micromechanical properties distinct from topographical cues across a number of ECM proteins. We determined that human fibroblasts and glioblastoma (GBM) cancer cells respond to topographical cues independently of tissue mechanics and type of ECM. Our results suggest that normal and cancer cells use similar machinery to respond to topography and provide a target for therapeutic intervention.

RESULTS

bioRxiv preprint doi: https://doi.org/10.1101/232066; this version posted December 10, 2017. The copyright holder for this preprint (which was not certified by peer review) is the author/funder, who has granted bioRxiv a license to display the preprint in perpetuity. It is made available under aCC-BY-NC-ND 4.0 International license.

Humanization of the nanofiber alignment system shows that normal cells respond to alignment for human ECM proteins

Overabundance of several ECM proteins is associated with abnormal tissue pathology(2). In the case of cancer, tumor-conditioned stromal cells at both sites of primary tumors and metastases secrete copious amounts of proteins. Specifically, astrocytes secrete tenascin C within the brain, whereas fibroblasts secrete fibronectin in response to tumor derived cytokines(41-43). Therefore, physiologically relevant biomaterials models would ideally incorporate both human cells and human matrix proteins. To translate our previously described biomaterials system to a more relevant humanized system, we first established that the three-dimensional fibrillar architecture system could be successfully used with human cells and human ECM proteins**).** Human ECM proteins were labeled with a fluorescent marker (**Supplementary Figure 1A**) and conjugated to 300 nm-diameter carboxylated superparamagnetic particles (**Supplementary Figure 1B**). To generate 3D matrices with embedded cells and fibers, cells were mixed with Matrigel and nanoparticles and plated in coverslip-bottom chamber slides that had been previously covered with a thin layer of gelled Matrigel. The slide was then either placed on a magnet to generate aligned fibrils or kept far from the magnet to maintain a random dispersion of particles. Finally, the slide was kept at 37°C to gel and set the nanoparticle topography, and cells were incubated in the presence of serum free medium for 24 h (**Figure 1A, Supplementary Figure 1C**).

We first characterized the mechanical properties of both aligned and unaligned matrices in the absence of cells. Gels were examined via parallel plate small angle oscillatory shear (SAOS) bulk rheology (**Figure 1B-D**). Bulk rheological measurements revealed that the complex moduli ($G^* = G' + iG''$, where G' = elastic component and G'' = viscous component) of aligned vs

bioRxiv preprint doi: https://doi.org/10.1101/232066; this version posted December 10, 2017. The copyright holder for this preprint (which was not certified by peer review) is the author/funder, who has granted bioRxiv a license to display the preprint in perpetuity. It is made available under aCC-BY-NC-ND 4.0 International license.

unaligned (random) matrices were comparable independently of the ECM coating used **(Figure 1B-D).** These hydrogels were mostly elastic, where the shear elastic moduli ranged from 10-30 Pa with very little viscous component over the range of ~0.1-100Hz (**Figure 1B**).

To obtain a baseline characterization of cell behavior as a function of matrix dimensionality, human foreskin fibroblast (HFF) cells were plated on a 2D surface and within a 3D Matrigel matrix lacking added nanoparticles. HFF cells were able to extend protrusions on 2D dishes coated with Matrigel, although with distinct morphology from cells in 3D. On 2D surfaces, cells formed broad lamellopodia, and stress fibers were clearly visible after staining for F-actin with a fluorescent phalloidin dye (**Figure 1E**). In Matrigel matrices lacking nanoparticles, HFF cells extended thin, filopodia-like protrusions but did not show the elongated morphology characteristic of fibroblasts on 2D surfaces (**Figure 1F**).

Fibrillar matrix formation and cell response were then tested using nanoparticles conjugated to human fibronectin, tenascin C, and laminin prior to fiber assembly in Matrigel in the presence of HFF cells. As an additional control using a protein lacking binding moieties for cell adhesion proteins, matrices containing bovine serum albumin (BSA)-conjugated nanoparticles were generated. For all proteins examined, oriented fibers were formed following magnetic alignment (fibers displayed in green; **Figure 1G**). In these aligned matrices, large (on the order of mm) areas could be patterned to contain oriented fibers with exposed ECM proteins for cell binding (**Supplementary Figure 2**). Fibroblasts embedded in patterned matrices were spindle shaped and could form long, actin-rich protrusions, as indicated by staining with phalloidin (displayed in red). In contrast, cells embedded in matrices containing unaligned nanoparticles (and thus, the same absolute amount of human ECM proteins) remained largely spherical (**Figure 1H**). Some particle aggregation was observed in unaligned matrices, but in general, the fluorophore

bioRxiv preprint doi: https://doi.org/10.1101/232066; this version posted December 10, 2017. The copyright holder for this preprint (which was not certified by peer review) is the author/funder, who has granted bioRxiv a license to display the preprint in perpetuity. It is made available under aCC-BY-NC-ND 4.0 International license.

density of the dispersed nanoparticles was not sufficient to generate a fluorescent signal. Cell shape in unaligned matrices was similar to that of cells embedded in Matrigel alone (**Figure 1F, H**).

Microscale mechanics are dependent on fiber formation and proximity in aligned fibrillar environments

In addition to topographical cues, cellular migration and cell morphology are sensitive to the compliance and viscoelasticity of their immediate milieu(2, 19). Macroscale mechanics are often determined from models where the material can be assumed to act as a continuum. In order for the continuum assumption to apply, the characteristic length scale of underlying structural components must be much smaller than that of the physical measurement(44). One concern relevant to characterization of the composite matrices is that the magnetic particles forming the aligned fibrils are rigid. Thus, we reasoned that at the microscale, the self-assembled fibrils may give rise to local variations in mechanics that will not be resolved with bulk rheology. We performed optical tweezer-based active microrheology to probe heterogeneous mechanical properties in 3D microenvironments on the length scales of cellular mechanotransduction (**Figure 2A-D**). The nature of these measurements enables us to spatially resolve effects of individual fibers on the surrounding amorphous gel by mapping the mechanical response from beads residing at increasing distances from the nearest fiber. For active microrheology experiments, composite gels containing fibronectin-conjugated nanoparticles were used. Active microrheology measurements revealed a gradient in the complex modulus as a function of distance from the assembled fiber (**Figure 2A,B; Supplementary Figure 3**). Regions within 1 μm of the fibers, which were comprised of rigid paramagnetic particles, were stiffer than the unaligned gels, with G* over 3-15,000 Hz ranging from 0.5 – 2.5 kPa and 0.2 – 2.0 kPa for aligned and unaligned gels, respectively, with both frequency ($p = 2.8e-80$) and fiber alignment ($p = 1.5e-39$) having

bioRxiv preprint doi: https://doi.org/10.1101/232066; this version posted December 10, 2017. The copyright holder for this preprint (which was not certified by peer review) is the author/funder, who has granted bioRxiv a license to display the preprint in perpetuity. It is made available under aCC-BY-NC-ND 4.0 International license.

statistically significant effects on G* by two-way ANOVA (**Figure 2A,B)**. At further distances of 2–4 μm from the nearest fiber, local stiffness decreased (**Figure 2A,B**). Complex modulus values at distances of 2–4 μm from the nearest fiber were slightly less those than in unaligned gels (**Figure 2A,B**). The complex modulus at a frequency of 3 Hz was 65 Pa, 100 Pa, and 175 Pa for beads at distances 2 μm, 3 μm, and 4 μm, respectively, while the complex modulus at 15,000 Hz was 300 Pa, 400 Pa, and 600 Pa for these distances. The effect of distance from the fiber on complex modulus across frequencies is summarized in **Figure 2B**. Interestingly, there was a distinct difference in frequency dependence of the complex moduli in aligned vs. unaligned gels **(Figure 2A,C; Supplementary Figure 3).** To quantitatively assess the frequency dependence of the complex moduli in these gels, we fit the complex modulus using a power law model, $G^*(\omega)=A\omega^b$, where ω is the frequency. For beads 1–4 μm away from an aligned fiber, the frequency dependence was similar, with G* weakly dependent on frequency, having power law fits of – 1 μm: A=194 (95% C.I.: 147, 241) , b=0.24 (95% C.I.: 0.21, 0.27), r^2: 0.95; 2 μm: A=35 (95% C.I.: 24, 36), b=0.24 (95% C.I.: 0.20, 0.28), r^2: 0.92; 3 μm: A=42 (95% C.I.: 26, 59), b=0.25 (95% C.I.: 0.21, 0.30), r^2: 0.90; 4 μm: A=30 (95% C.I.: 21, 38), b=0.22 (95% C.I.: 0.18, 0.25), r^2=0.91). Interestingly, in unaligned gels, the power law exponents were closer to the value (0.75) predicted for semi-flexible polymers (A=5 (95% C.I.: 2, 8), b=0.61 (95% C.I.: 0.54, 0.68), r^2: 0.98). In addition, the frequency dependence of the elastic and viscous contributions to the complex moduli differed between the aligned and unaligned gels, with crossover frequencies (at which G'' first exceeds G') of ~1 kHz in unaligned gels and ~10 kHz in aligned gels (**Supplementary Figure 3C**). As an example, the crossover frequency in aligned matrices at a distance of 3 μm from the nearest fiber was much greater than that in unaligned gels (**Figure 2C**). Importantly, in the low

bioRxiv preprint doi: https://doi.org/10.1101/232066; this version posted December 10, 2017. The copyright holder for this preprint (which was not certified by peer review) is the author/funder, who has granted bioRxiv a license to display the preprint in perpetuity. It is made available under aCC-BY-NC-ND 4.0 International license.

frequency regime, bulk and microrheology methods gave nearly identical values for the complex modulus (**Figure 2D**).

Having determined that there are local heterogeneities in microscale mechanics, we next sought to determine how cells would respond to substrates of differing mechanical properties. We reasoned that a "2D" geometry approximates the cues that cells receive when they co-opt aligned fibers. Previous work has shown that sensitivity to ECM substrate stiffness is dependent on the concentration of ECM ligand(16, 45). Thus, we compared cells seeded on substrates that span several orders of magnitude from 0.2kPa->GPa for a comparable concentration of ECM protein. This dynamic range allowed us to probe responses across the stiffnesses of several tissues, from the brain to the bone. To examine the differential response of normal and cancer cells for a given ECM condition, we used HFF cells and a human glioblastoma cell line (U87) in our system. We determined that HFF and U87 cells were largely insensitive to the stiffness of the underlying ECM substrate, as determined by cell morphology and the presence of actin cytoskeletal structures **(Figure 2E)**. Substrate stiffness was not a significant source of variation in cell area or aspect ratio by two-way ANOVA, and significant differences in areas and aspect ratios were only seen between HFF cells on the much stiffer tissue culture plastic compared to some of the softer silicone substrates (**Figure 2F-G**).

Human foreskin fibroblasts and glioblastoma cells show an enhanced response to topographical cues for a myriad of human ECM proteins in the 3D microenvironment

Confident that cells were largely insensitive to a dynamic range of substrate stiffnesses for a given ECM concentration, we next asked if ECM composition or fibrillar architecture dictates cell response in 3D for both normal and transformed cells. To quantitatively characterize the response of human cells to the humanized nanofiber system, HFF cells were plated in aligned and

bioRxiv preprint doi: https://doi.org/10.1101/232066; this version posted December 10, 2017. The copyright holder for this preprint (which was not certified by peer review) is the author/funder, who has granted bioRxiv a license to display the preprint in perpetuity. It is made available under aCC-BY-NC-ND 4.0 International license.

unaligned matrices, fixed after 24 h, and imaged. HFF cells plated in aligned matrices preferentially sent out protrusions along or perpendicular to the fibers (**Figure 3A**). In contrast, cells remained spherical in unaligned matrices (**Figure 3B**). Timelapse videos of HFF cells embedded in aligned matrices revealed that cells typically sent out protrusions along or perpendicular to fibers before locally contracting the matrix (**Supplementary Video 1**). The length of protrusions of cells in aligned matrices 24 h after seeding significantly increased compared to cells in unaligned matrices, where protrusion lengths were similar to those seen in Matrigel alone (**Figure 3C**). The local angle between fibers and cell protrusions in aligned matrices was preferentially either 0° or 90° (**Figure 3D**), indicating protrusions sent out parallel or perpendicular to the fibers (see insets in **Figure 3A**). This preference was not observed in unaligned matrices, where protrusions were randomly distributed around the cell body (**Figure 3E**). These trends held across all of the ECM protein coatings tested, including BSA, suggesting that the presence of a topographical cue was more important in the observed cell extensions than specific integrin-ECM interactions. Although both ECM coating and matrix alignment were significant sources of variation by two-way ANOVA, matrix alignment status was the predominant factor, accounting for 46% of the observed variation, and protrusions were significantly longer in aligned vs. unaligned matrices for all ECM proteins tested.

We next asked if GBM cells would show similar responses to the diversity of tissue architectures and chemistries tested using human U87 cells. Identical behaviors were observed for U87 and HFF cells embedded in aligned vs. unaligned matrices (**Figure 3A-B, F-G**). Interestingly, U87 cells also extended longer protrusions in aligned than unaligned matrices for a given ECM protein (**Figure 3H**). Similar to the case seen in HFF cells, both ECM protein and alignment status were significant sources of variation in protrusion length by two-way ANOVA,

bioRxiv preprint doi: https://doi.org/10.1101/232066; this version posted December 10, 2017. The copyright holder for this preprint (which was not certified by peer review) is the author/funder, who has granted bioRxiv a license to display the preprint in perpetuity. It is made available under aCC-BY-NC-ND 4.0 International license.

but alignment status again accounted for the largest percentage of the variation observed. Finally, topographical cues in aligned matrices led to U87 cell protrusions predominantly parallel or perpendicular to local fibers (**Figure 3I**). These trends were not observed in unaligned matrices, where protrusions were again distributed around the cell body instead of in preferred directions (**Figure 3J**).

DISCUSSION

The ECM provides important chemical signals within native tissue(2, 19). In addition, physical properties of the microenvironment, such as tissue mechanics and surface topography, have been shown to modulate gene expression(2, 19). But how do cells respond to these external cues? Is there a hierarchy where one type of cue, physical vs. chemical, overrides the other? Where would such a distinction be valid? These concepts are often difficult to discern using naturally derived 3D tissue mimetics, as precise control of ligand density and architecture are often intertwined. Moreover, dissecting differential physical cues such as mechanics from architecture is also challenging. To address these questions, we previously described a method of self-assembly of nanofibrils in 3D hydrogels(17, 46). Briefly, paramagnetic colloidal particles functionalized with ECM proteins were exposed to an external magnetic flux to drive self-assembly of nanofibrils parallel to the direction of the external field. In this study, we fully humanized our model, where both cell type and ECM proteins reflect homotypic interactions mimicking human tissue. We also extended our list of ECM proteins to include proteins associated with organ-specific disease pathologies. These tissue mimetics recreate important aspects of complex in vivo geometries while independently controlling bulk stiffness and ECM ligand density. Here, microscale heterogeneities in stiffness due to the rigid magnetic particles was not

bioRxiv preprint doi: https://doi.org/10.1101/232066; this version posted December 10, 2017. The copyright holder for this preprint (which was not certified by peer review) is the author/funder, who has granted bioRxiv a license to display the preprint in perpetuity. It is made available under aCC-BY-NC-ND 4.0 International license.

the regulator of cell morphology. Instead, topographical cues were sufficient to guide morphologies of normal and tumor cells in 3D hydrogels.

To begin characterizing the hierarchy of external cues on cell phenotype, we investigated the roles of mechanics, ECM composition, and topography in our model system. Within a given microenvironment, cells respond to cues at different length scales, from nanoscale and microscale to longer-range cues. For example, fibroblasts generate and retract protrusions to sense the underlying substrate stiffness(36). The magnetic particles used here are rigid and thus will introduce local heterogeneities on the micrometer scale that may influence cell behavior. Using active microrheology, we resolved mechanical variations present within a few micrometers of assembled fibers in the matrix that was not resolved at the mm length scale using bulk rheology. Compared to beads measured in unaligned gels, beads within one micrometer of the nearest fiber in aligned gels were significantly more rigid, whereas rigidity decreased with distance at 2-4 μm and was lower than in unaligned gels, possibly owing to changes in local concentration in the background matrix due to interactions with the nanochain fibers. Microscale mechanics are dependent upon local mesh geometry(47). Thus, one reason may be that the mesh size of the defined fibrillar architecture differs from that in the unaligned hydrogels. In addition to differences in the magnitude of the complex modulus, we observed a difference in frequency dependence between the aligned gels and unaligned gels. Power law dependence of the complex modulus on frequency has been previously observed in a number of biomaterials, and various models have been proposed to explain this behavior according to the underlying dynamics of the constituent polymers (47-50). In fibrillar collagen gels polymerized at 2 mg/ml or 6 mg/ml at 4°C or 37°C, we previously observed power law exponents ranging from 0.66 – 0.74(48), in the range predicted for a semi-flexible polymer network. Here, we observed exponents of ~0.6 in unaligned gels but only

bioRxiv preprint doi: https://doi.org/10.1101/232066; this version posted December 10, 2017. The copyright holder for this preprint (which was not certified by peer review) is the author/funder, who has granted bioRxiv a license to display the preprint in perpetuity. It is made available under aCC-BY-NC-ND 4.0 International license.

~0.25 near fibers in aligned gels. Crossover frequencies at which G'' exceeds G' correspond to characteristic relaxation times and reflect the intrinsic time scale of energy dissipation processes inside the material. In the previously measured collagen gels, crossovers occurred at 300 Hz for the gels with fine mesh of small fibers and 2750 Hz for the gels with larger mesh and thicker, longer fibers(48). Here we observed unaligned gel crossovers at 1000 Hz and aligned gel crossovers at 10000 Hz.

Substrate stiffness has been shown to regulate cell morphology and motility(45, 49). Cells show reduced area and adhesion on substrates where the Young's Modulus is ~100Pa whereas both cell area and presence of strong focal adhesion formation increases as the substrate rigidity is increased (45). However, this response is dependent on the concentration of the ECM ligand density, thus showing the interdependence of chemical and physical cues in a regime dependent manner(45). At frequencies less than 500 Hz, the cell's environment varies ~ 5-fold when co-opting a fibrils vs embedded in unaligned gels. Here, we confirmed that both normal and cancer cells are insensitive to substrate stiffness for described given ligand concentration. This confirmed that our system will allow discernment of topographical and chemical cues in 3D. At frequencies greater than 500 Hz, few physiological processes such as ion channel gating have been documented that might be influenced by external cues in this dynamic range (50). Nevertheless, it remains to be seen how such a transition will modulate cell fate decisions.

We next addressed the role of ECM chemical cues on cell phenotype in our system. Other studies have elegantly elucidated role of adhesion-scale ECM presentation and integrin binding(51). For example, simulations of stretching of a module of a FN fibril, FN III, is sufficient to override integrin beta one-dependent modulation of increased ligand binding and associated down-stream signaling(52). Integrins act as the transmembrane anchor between the cell and the

bioRxiv preprint doi: https://doi.org/10.1101/232066; this version posted December 10, 2017. The copyright holder for this preprint (which was not certified by peer review) is the author/funder, who has granted bioRxiv a license to display the preprint in perpetuity. It is made available under aCC-BY-NC-ND 4.0 International license.

ECM. Heterodimers of an alpha subunit and beta subunit are used by the cells for specificity of ECM binding. FN, tenascin-C, and laminin are known to be ligands for beta 1 integrin with alpha subunits of alpha5, alpha6, and alpha9, respectively(20, 41, 43). We confirmed that human cells co-opted Nano fibrils independently of the surface coating of the magnetic particles, including BSA as a control, thus showing conservation of our previous finding. Specifically, we showed that both normal and cancer cells respond to topographical cues independently of chemical ligand. Cells respond where cell body and protrusions were perpendicular to the nanogrooves between paramagnetic particles and parallel to the microns-length aligned chains of the assembled fibrils, consistent with observation for hybrid topographies. For both HFF and U87 cells, the protrusion length in the randomly oriented hydrogel was comparable to the control gel with no particles. However, fibroblasts extended longer protrusions in aligned matrices for each protein observed. In the case of the GBM cells, protrusions were marginally longer for FN compared to the other proteins probed. These results suggest that tumor cells may also use a similar mechanism to respond to topography as normal mesenchymal cells. However, we cannot rule out that cells behaved similarly simply as these cells may be using the same receptor to bind to these proteins.

Finally, cell-scale ECM architecture has been shown to regulate force transmission between cells and the environment, gene expression, development, and cell motility(53, 54). Tissue anisotropy is thought to provide guidance for cell protrusion and cell motility in both normal and diseased pathologies. Not restricted to post-embryonic stages, seminal work showed that spinal neurons of a frog embryo co-aligned with the underlying architecture of a spider web(55). In normal tissue homeostasis, extensions and protrusions for neurons and fibroblasts often co-align in the direction of ECM fibers. Tumor cells also use aligned fibrillar structures for rapid and widespread dissemination from the primary site(56). In the case of breast cancer, radially aligned

bioRxiv preprint doi: https://doi.org/10.1101/232066; this version posted December 10, 2017. The copyright holder for this preprint (which was not certified by peer review) is the author/funder, who has granted bioRxiv a license to display the preprint in perpetuity. It is made available under aCC-BY-NC-ND 4.0 International license.

collagen type 1 is associated with poor prognosis(30). In concert with murine models, it is thought that cells are able to use the fibrils as "highways" to facilitate rapid intravasation. Not restricted to the breast, GBM cells diffuse throughout the brain parenchyma, preferentially migrating along blood vessels and fiber tracts(31). These cues are yet to be fully understood in the context of tumor cell survival and drug efficacy as observed for tumor cells that grow along blood vessels.

For in vitro studies, surface cues such as microgrooves, ridges, and patterned substrates have been used to show that cells modulate signaling cascades and gene expression in 2D platforms in response to topography(56, 57). Additionally, naturally derived ECMs such as collagen and fibrin can be used to form diverse fibrillar architectures in 3D hydrogels(58). However, tissue mechanics and local ligand density are often coupled in these systems. Using the 3D fiber self-assembly process described here in concert with controlled ECM protein coatings and micromechanical matrix characterization, we were able to dissect the contributions of the physical properties from those due to chemical properties on cell fate as it relates to malignancy and normal tissue homeostasis. We discovered that topographical cues dominated cell behavior for a myriad of human ECM proteins implicated in disease pathology, and did so independently of bulk and microscale tissue mechanics. These data suggest that topography may override both ECM chemical and physical cues when ECM concentrations sufficiently override sensitivity to substrate stiffness. This work defines a regime in which a clear hierarchy of cues is established in driving cell fate and behavior. This platform can then be used to delineate how these cues influence downstream signaling to influence cell survival, a missing signal in decoupling the role of tissue architecture on tumor cell survival in vivo.

ACKNOWLEDGMENTS

bioRxiv preprint doi: https://doi.org/10.1101/232066; this version posted December 10, 2017. The copyright holder for this preprint (which was not certified by peer review) is the author/funder, who has granted bioRxiv a license to display the preprint in perpetuity. It is made available under aCC-BY-NC-ND 4.0 International license.

This research was supported by the Intramural Research Program of the National Institutes of Health, the National Cancer Institute. We thank Daniel Blair and Xinran Zhang and the Institute for Soft Matter Synthesis and Metrology at Georgetown University for access to and assistance with bulk rheology measurements. We also thank Ken Yamada, NIDCR, NIH for the kind gift of HFF cell lines. We thank Jayne Stommel, NCI, NIH for U87 cell lines. A. Hruska received a NIH GSOAR Summer fellowship.

MATERIALS AND METHODS

Cell culture

Human foreskin fibroblast cells were cultured in Dulbecco's Modified Eagles Medium (DMEM) supplemented with 10% fetal bovine serum, 1% penicillin-streptomycin, and 1% L-glutamine and maintained at 37°C and 10% CO_2. Cells were sub-passaged every 2-3 days.

Conjugation of fluorophores to human proteins

To study human cell recognition of human proteins, several proteins were used. Human laminin (pepsinized; EMD Millipore, AG56P), human collagen type I (EMD Millipore, CC050), human tenascin-C (EMD Millipore, CC065), and human plasma fibronectin (EMD Millipore, FC010) were conjugated to fluorophores using the DyLight™ 488 Microscale Labeling Kit (ThermoFisher, 53025) according to the manufacturer's instructions. Briefly, proteins were supplied in suspension at concentrations ranging from 0.25-1 mg/ml. Laminin and tenascin-C were at concentrations less than recommended for labeling (0.5 mg/ml and 0.25 mg/ml, respectively; suggested concentration for conjugation to fluorophore is 1 mg/ml). For these proteins, 50 μg and 25 μg, respectively, were used in the labeling reaction instead of the recommended 100 μg. Bovine

bioRxiv preprint doi: https://doi.org/10.1101/232066; this version posted December 10, 2017. The copyright holder for this preprint (which was not certified by peer review) is the author/funder, who has granted bioRxiv a license to display the preprint in perpetuity. It is made available under aCC-BY-NC-ND 4.0 International license.

serum albumin (BSA) dissolved in PBS at a concentration of 1 mg/ml was also labeled for use as a control that does not specifically bind to cell adhesion proteins. Following labeling, protein concentrations were measured using a DeNovix DS-11+ Spectrophotometer and the "Labeled Protein" module. E1% was set at 10 g/100 ml, A = 1 mg/ml, with analysis wavelength for fluorescence at 494 nm, extinction coefficient set at 71,000, A260 factor of 0.3, and A280 factor of 0.11. Successful labeled was indicated by an absorption peak at 494 nm.

Conjugation of proteins to magnetic nanoparticles

Labeled proteins were conjugated to 300-nm diameter paramagnetic nanoparticles as described previously using the Ademtech Carboxy-Adembeads Coupling Kit (Ademtech, 02820)(17). Briefly, 0.5 mg of carboxylated superparamagnetic nanoparticles were washed in Activation Buffer, activated with EDC, and incubated with 20 µg of fluorescently-labeled protein overnight under gentle shaking. Then, 200 µl of 0.5 mg/ml BSA in Activation Buffer was used to quench the reaction. Functionalized beads were washed three times with Storage Buffer, and beads were then stored at a final concentration of 1 mg/ml in Storage Buffer at 4°C for up to 2 weeks.

Cell seeding and topographic alignment in 3D matrices

Matrigel (BD Corning, 356230) was thawed on ice and maintained at 4°C. Prior to experiments, Matrigel was stored on ice to reach a stable temperature. A 100 µl aliquot of Matrigel was spread uniformly over the surface of a Lak-Tek 4-well chambered coverglass well (ThermoScientific, 155383) chilled on ice and placed in an incubator at 37°C for 5 minutes to polymerize. Prior to seeding in 3D culture, HFF or U87 cells were washed with phosphate buffered saline (PBS), detached from the cell culture flask using 10 mM EDTA in PBS, washed once in growth medium, centrifuged at 1000 rpm for 5 min, and resuspended to a concentration of 2 x 10^6

bioRxiv preprint doi: https://doi.org/10.1101/232066; this version posted December 10, 2017. The copyright holder for this preprint (which was not certified by peer review) is the author/funder, who has granted bioRxiv a license to display the preprint in perpetuity. It is made available under aCC-BY-NC-ND 4.0 International license.

cells/ml in serum-free medium. Cells were then mixed with functionalized nanoparticles and Matrigel in the following ratio: 12 µl beads at a concentration of 1 mg/ml, 430 µl Matrigel, and 50 µl cell suspension (100,000 cells).

The mixture was gently mixed by pipette, and 400 µl of this mixture was added to a well of the 4-well coverslide. For alignment of the nanoparticles, the slide was immediately placed on a magnet (NdFeB magnet, K&J Magnetics, BX8X8X8, 25.4 mm x 25.4 mm x 25.4 mm) chilled in ice for 15 minutes. Following alignment, the slide was placed in the 37°C incubator for 30 minutes to polymerize the Matrigel. For unaligned topographies, slides were placed on ice far from the magnet for 15 minutes following the addition of the cell/nanoparticle/Matrigel mixture and then polymerized for 30 minutes at 37°C. Wells on the slides were seeded sequentially to ensure proper nanoparticle alignment over the center of the magnet, where field lines are parallel. Following Matrigel polymerization, 350 µl of serum-free medium was added to each well. Slides were placed in the incubator for 24 h prior to fixation. As a control, an equal number of cells was seeded in a Matrigel matrix, where the 12 µl bead mixture was replaced with pure Matrigel, resulting in a matrix containing cells but no additional ECM-conjugated nanoparticles. As an additional control, the 2D surface of a 4-well slide was coated with Matrigel proteins by covering the base of the well with 100 µl Matrigel, maintaining the Matrigel in liquid form on ice for 1 h, aspirating the Matrigel, and washing the slide surface in triplicate with PBS. To analyze 2D morphology, 100,000 cells in serum free medium was added to the well, which was incubated for 24 h.

Bulk rheology

Small angle oscillatory shear bulk rheology measurements were carried out at the Georgetown University Institute for Soft Matter Synthesis and Metrology using an Anton Paar

bioRxiv preprint doi: https://doi.org/10.1101/232066; this version posted December 10, 2017. The copyright holder for this preprint (which was not certified by peer review) is the author/funder, who has granted bioRxiv a license to display the preprint in perpetuity. It is made available under aCC-BY-NC-ND 4.0 International license.

Physica MCR 301 rheometer equipped with a PP-25 measuring plate (parallel, 25 mm diameter). Gels were polymerized on 50 mm glass bottom dishes (WillCo, GWSB-5040). Samples were prepared with 120 µl Matrigel on bottom of WillCo dish polymerized prior to the Matrigel/bead matrix. To this, a mixture of 430 µl Matrigel, 30 µl SFM, 12 µl paramagnetic beads, and 20 µl of $1x10^5$/ml polystyrene beads ($2x10^6$ beads total). Samples were either aligned or unaligned as described above and were hydrated with a superlayer of media for storage and transport. Media was removed with a pipette before measurements. The instrument achieved contact with the sample with a trigger force of 0.1 N normal and the excess gel was trimmed around the plate to ensure proper contact boundary conditions. The complex modulus was measured at 1% strain at frequencies 0.1-10 Hz. Measurements were carried out in duplicate. In Figure 1D, for each measured frequency, the mean complex modulus was divided by the mean complex modulus in unaligned gels, and moduli are expressed as percentages of the unaligned gel complex modulus (mean ± standard deviation) across all frequencies.

Optical tweezer-based microrheology

Samples were prepared in WillCo dishes identically to those made for bulk rheology measurements prior to characterization via optical tweezer-based microrheology. For complete experimental details, see(48, 59, 60). Our home-built setup consists of a 1064 nm trapping beam steered by an acousto-optic deflector to oscillate the trap and a stationary 975 nm detection beam that is coupled into and colocated with the trap with a dichroic before being sent into the backport of an inverted microscope with a long working distance water objective and a high NA condenser. Telescope lenses conjugate the optical plane at the acousto-optic deflector (AOD) to the back aperture of the condenser, which is placed in Kohler illumination after the object is focused in the specimen place. Above the condenser, the detection beam is relayed to a quadrant photodiode for

bioRxiv preprint doi: https://doi.org/10.1101/232066; this version posted December 10, 2017. The copyright holder for this preprint (which was not certified by peer review) is the author/funder, who has granted bioRxiv a license to display the preprint in perpetuity. It is made available under aCC-BY-NC-ND 4.0 International license.

back focal plane interferometric position detection. Each bead is positioned precisely in the center of the trap by scanning it through the detection beam in three dimensions using a piezo nanopositioning stage while recording the voltages from the QPD. The V-nm relation of the QPD is calibrated in situ by fitting the central linear region of the detector response to scanning the bead through the detection beam in the direction of the oscillations, giving β in V/nm (stuck bead method). A second QPD records the position of the trapping laser to find the relative phase lag between the bead and trap oscillations. The optical trap stiffness k is determined in situ from the thermal power spectrum of each measured bead while the trap is stationary, using the active-passive calibration method(61). Together with β, k, and the bead's mass m and radius a, the trajectories yield the complex modulus as a function of frequency, G*(ω), of each bead's surrounding microenvironment. In this equation, the complex modulus, G*(ω), can be broken down into components, with $G^*(\omega) = G'(\omega) + iG''(\omega)$, where the real part, G'(ω), is the elastic component and the imaginary part, G''(ω), is the viscous component. The complex modulus, G*(ω), is calculated as $G^*(\omega) = \frac{i\omega\tilde{\gamma}_D(\omega)}{6\pi a}$, where the friction relaxation spectrum $\tilde{\gamma}_D(\omega)$ is related by the equation $\tilde{\gamma}_D(\omega) + i\omega m = -\frac{k}{i\omega}\left(\frac{1}{i\omega\tilde{R}_L(\omega)} + 1\right)$ to the active power spectrum $\tilde{R}_L(\omega) \equiv \frac{\tilde{x}_{dr}(\omega)}{-i\omega\tilde{x}_L(\omega)}$, with $\tilde{x}_L(\omega)$ and $\tilde{x}_{dr}(\omega)$ the Fourier transforms of the time series of the positions of the trapping laser and the driven bead respectively, recorded while the trap is oscillating. The stiffness $k = \frac{\mathrm{Re}\{\tilde{R}_L(\omega)\}}{P_U(\omega)}$ is determined from the real part of the active power spectrum and the passive power spectrum, $P_U(\omega) \equiv \left\langle \left|\tilde{x}_U(\omega)\right|^2 \right\rangle$, where $\tilde{x}_U(\omega)$ is the Fourier transform of the time series of the undriven bead's thermally fluctuating position while the trap is held stationary. Each bead is subjected to fourteen consecutive 2 s pulses, with the trap alternately oscillating or stationary. Amplitude of oscillations

bioRxiv preprint doi: https://doi.org/10.1101/232066; this version posted December 10, 2017. The copyright holder for this preprint (which was not certified by peer review) is the author/funder, who has granted bioRxiv a license to display the preprint in perpetuity. It is made available under aCC-BY-NC-ND 4.0 International license.

was set to 20 nm with power of 100 mW at the back aperture. Only probes at distances exceeding ~30 μm away from the cover slip surface to minimize drag in consideration of Faxen's law were measured (62).

Samples were measured in triplicate with at least 30 beads per sample measured. Laser power was set to 100mW at the back aperture. Data were analyzed using custom MATLAB programs. Experiments were controlled using custom LabVIEW programs. For each distance from the nearest fiber and each measured frequency, the mean complex modulus was divided by the mean complex modulus in unaligned gels. In Figure 2B, for each distance from the nearest fiber and each measured frequency, the mean complex modulus was divided by the mean complex modulus in unaligned gels, and moduli are expressed as percentages of the unaligned gel complex modulus. These percentages were averaged across all frequencies to obtain the plotted means and standard deviations.

Cell seeding on 2D silicone substrates of known elastic modulus

Cytosoft 6-well plates (Advanced Materials, 5190-7EA; 0.5 kPa, 2 kPa, and 64 kPa elastic modulus) or standard 6-well tissue culture plastic dishes were incubated with human plasma fibronectin (EMD Millipore, FC010) at a concentration of 10 μg/ml diluted in PBS (3 ml/well of ECM protein solution added) for 1 h at room temperature. The coating solution was aspirated, and wells were washed twice with PBS. HFF or U87 cells were washed with phosphate buffered saline (PBS), detached from the cell culture flask using 10 mM EDTA in PBS, washed once in growth medium, centrifuged at 1000 rpm for 5 min, and resuspended to a concentration 100,000 cells/ml in serum free medium. To each well, 1 ml of the cell suspension (100,000 cells total) and 1 ml of serum free media were added. Plates were incubated overnight at 37°C prior to fixation and staining.

bioRxiv preprint doi: https://doi.org/10.1101/232066; this version posted December 10, 2017. The copyright holder for this preprint (which was not certified by peer review) is the author/funder, who has granted bioRxiv a license to display the preprint in perpetuity. It is made available under aCC-BY-NC-ND 4.0 International license.

Cell fixation and fluorescent staining

For samples embedded in Matrigel matrices, media was aspirated, and each well was washed with 200 µl PBS. To each well, 300 µl of 4% paraformaldehyde diluted in PBS was added, and samples were incubated for 3 hours at room temperature. Samples were incubated with 300 µl/well of 1% BSA in PBS at room temperature for 30 minutes to block non-specific binding. A phalloidin stock solution was prepared by dissolving 10 nmol of phalloidin-Atto 565 (Sigma, 94072-10NMOL) in 500 µl methanol. To fluorescently label F-actin and the nucleus, a solution containing 2 µg/ml Hoechst 33258 (Molecular Probes, H3569) and 30 µl phalloidin stock/ml in 1% BSA in PBS was prepared. Cells were stained with 200 µl/well of the staining solution at room temperature for 3 h, then washed three times with 200 µl/well PBS. Samples were stored in PBS at 4°C prior to imaging.

For samples plated on substrates of varying stiffness, culture media was aspirated, and 3 ml of 4% paraformaldehyde diluted in PBS was added to each well. Samples were fixed at room temperature for 15 min and washed twice with PBS. Cells were then permeabilized with 0.1% Triton X-100 in PBS for 5 min and washed twice more with PBS. A phalloidin stock solution was prepared by dissolving 10 nmol of phalloidin-Atto 488 (Sigma, 49409-10NMOL) in 500 µl methanol. To fluorescently label F-actin and the nucleus, a solution containing 1 µg/ml Hoechst 33258 (Molecular Probes, H3569) and 20 µl phalloidin stock/ml in 1% BSA in PBS was prepared. Cells were stained with 500 µl staining solution/well for 1 h at room temperature. Finally, wells were washed twice with PBS and stored in PBS prior to imaging. For each condition, two wells per cell type were prepared simultaneously.

Imaging

bioRxiv preprint doi: https://doi.org/10.1101/232066; this version posted December 10, 2017. The copyright holder for this preprint (which was not certified by peer review) is the author/funder, who has granted bioRxiv a license to display the preprint in perpetuity. It is made available under aCC-BY-NC-ND 4.0 International license.

For cells embedded in 3D matrices, images were acquired on a Zeiss 780 LSM confocal microscope. One-photon, confocal, 12-bit, 2-dimensional images were acquired at lateral dimensions of 512x512 pixels with a Zeiss 20x Plan-Apochromat, 0.8 NA objective. Individual images were tiled (3x3 grid) to image a total area of 1275.29 μm x 1275.29 μm (1536 pixels x 1536 pixels). Tiled images were acquired in z-stacks spaced 2 μm apart over an axial distance of ~120 μm to image cells throughout the matrix. Samples were excited with 561 nm light from a solid-state laser with a total power of 20 mW, 405 nm light from a laser diode with a total power of 30 mW, and 488 nm light from an argon laser with a total power of 25 mW. Lasers were set at or below 2.4% of the total power. Two beam splitters, MBS 488/561 and MBS 405, were employed in the emission pathway to delineate the red, green, and blue channels. Transmitted light was also collected. Pinhole width was set at 90 μm. Pixel dwell was set at 1.58 μs. The master gain was set at or below 890 for all images acquired. For the images displayed in Figure 3 and a subset of the images displayed in Figure 1, confocal z stacks were acquired at 2048 pixels x 2048 pixels to obtain greater detail of cell and fiber morphology.

For cells plated on 2D silicone substrates, imaging was carried out at 20x magnification using a ThermoFisher EVOS FL Cell Imaging System. Four random fields of view were selected for each well. Two wells were prepared and imaged simultaneously for each cell type and substrate stiffness. A minimum of 103 cells were imaged and analyzed for each condition.

Analysis of cell morphology on 2D substrates

Cell morphology on 2D substrates of varying elastic modulus was analyzed using Fiji. Images obtained from the F-actin channel were binarized using the default Fiji settings and processed using the "Close-" function in Fiji. Dead and truncated cells were removed from the images, and shapes were manually separated or joined when necessary to more closely match the

bioRxiv preprint doi: https://doi.org/10.1101/232066; this version posted December 10, 2017. The copyright holder for this preprint (which was not certified by peer review) is the author/funder, who has granted bioRxiv a license to display the preprint in perpetuity. It is made available under aCC-BY-NC-ND 4.0 International license.

original images. Another investigator compared the final drawings to the original images for independent verification of the results. Circularity and area were calculated from the binarized images using the "Analyze Particle" function in Fiji. Measurements were made on cells in four random fields of view for each well, with two wells per substrate elastic modulus prepared and imaged simultaneously for each cell type. Statistics were carried out and plots were generated in GraphPad Prism 7. The effects of cell type and matrix stiffness on cell area and aspect ratio were analyzed using two-way ANOVA with Tukey's multiple comparisons post-tests between all combination of substrate stiffnesses for a given cell type.

Protrusion analysis for cells embedded in 3D matrices

To analyze protrusion length and directionality, confocal tile scans acquired at 20x magnification and axial steps of 2 µm (1275.29 µm x 1275.29 µm, 1536 pixels x 1536 pixels) were opened in Fiji, and the transmitted and actin channels were displayed. Protrusions were measured only in the plane in which the fibers were in focus to quantify cell response to local fibers in aligned matrices, and only for cells clearly embedded in 3D for unaligned matrices. The line tool in Fiji was used to draw a line from the center of the cell (manually identified) to the end of the protrusion to measure the protrusion length and protrusion angle. In aligned matrices, the line tool was also used to draw a line on the fiber immediately adjacent to the protrusion. The angle (0°-90°) between the protrusion and the neighboring fiber was calculated and recorded as the protrusion angle. For cells in unaligned matrices, the protrusion angle was calculated with respect to the vertical, and all angles were then mapped to be between 0° and 90°. For each cell type, matrix alignment status, and nanoparticle ECM protein, 20 protrusions were measured from a single 3D matrix. Statistical analysis and plot generation were done in Prism GraphPad 7. Histograms were generated to visualize the distribution of protrusion angles in aligned and unaligned matrices. Protrusion lengths

bioRxiv preprint doi: https://doi.org/10.1101/232066; this version posted December 10, 2017. The copyright holder for this preprint (which was not certified by peer review) is the author/funder, who has granted bioRxiv a license to display the preprint in perpetuity. It is made available under aCC-BY-NC-ND 4.0 International license.

were compared between aligned and unaligned matrices using Sidak's multiple comparisons test between aligned and unaligned protrusions for a given ECM nanoparticle coating following two-way ANOVA.

bioRxiv preprint doi: https://doi.org/10.1101/232066; this version posted December 10, 2017. The copyright holder for this preprint (which was not certified by peer review) is the author/funder, who has granted bioRxiv a license to display the preprint in perpetuity. It is made available under aCC-BY-NC-ND 4.0 International license.

REFERENCES

1. Kumar S & Weaver VM (2009) Mechanics, malignancy, and metastasis: the force journey of a tumor cell. *Cancer Metastasis Rev* 28(1-2):113-127.
2. Lu P, Weaver VM, & Werb Z (2012) The extracellular matrix: a dynamic niche in cancer progression. *J Cell Biol* 196(4):395-406.
3. Tanner K & Gottesman MM (2015) Beyond 3D culture models of cancer. *Sci Transl Med* 7(283):283ps289.
4. Tenney RM & Discher DE (2009) Stem cells, microenvironment mechanics, and growth factor activation. *Curr Opin Cell Biol* 21(5):630-635.
5. Xu R, Boudreau A, & Bissell MJ (2009) Tissue architecture and function: dynamic reciprocity via extra- and intra-cellular matrices. *Cancer Metastasis Rev* 28(1-2):167-176.
6. Bischel LL, Beebe DJ, & Sung KE (2015) Microfluidic model of ductal carcinoma in situ with 3D, organotypic structure. *BMC Cancer* 15:12.
7. Chaudhuri O*, et al.* (2014) Extracellular matrix stiffness and composition jointly regulate the induction of malignant phenotypes in mammary epithelium. *Nat Mater* 13(10):970-978.
8. Engler AJ, Sen S, Sweeney HL, & Discher DE (2006) Matrix elasticity directs stem cell lineage specification. *Cell* 126(4):677-689.
9. Levental KR*, et al.* (2009) Matrix crosslinking forces tumor progression by enhancing integrin signaling. *Cell* 139(5):891-906.
10. Lin CH*, et al.* (2015) Microenvironment rigidity modulates responses to the HER2 receptor tyrosine kinase inhibitor lapatinib via YAP and TAZ transcription factors. *Mol Biol Cell* 26(22):3946-3953.
11. Mouw JK*, et al.* (2014) Tissue mechanics modulate microRNA-dependent PTEN expression to regulate malignant progression. *Nat Med* 20(4):360-367.
12. Paszek MJ*, et al.* (2005) Tensional homeostasis and the malignant phenotype. *Cancer Cell* 8(3):241-254.
13. Provenzano PP*, et al.* (2012) Enzymatic targeting of the stroma ablates physical barriers to treatment of pancreatic ductal adenocarcinoma. *Cancer Cell* 21(3):418-429.
14. Provenzano PP*, et al.* (2006) Collagen reorganization at the tumor-stromal interface facilitates local invasion. *BMC Med* 4(1):38.
15. Provenzano PP, Eliceiri KW, Inman DR, & Keely PJ (2010) Engineering three-dimensional collagen matrices to provide contact guidance during 3D cell migration. *Curr Protoc Cell Biol* Chapter 10:Unit 10 17.
16. Pathak A & Kumar S (2012) Independent regulation of tumor cell migration by matrix stiffness and confinement. *Proc Natl Acad Sci U S A* 109(26):10334-10339.
17. Kim J, Staunton JR, & Tanner K (2016) Independent Control of Topography for 3D Patterning of the ECM Microenvironment. *Adv Mater* 28(1):132-137.
18. Kim J & Tanner K (2015) Recapitulating the Tumor Ecosystem Along the Metastatic Cascade Using 3D Culture Models. *Front Oncol* 5:170.
19. Ross AM, Jiang Z, Bastmeyer M, & Lahann J (2012) Physical aspects of cell culture substrates: topography, roughness, and elasticity. *Small* 8(3):336-355.
20. Mao Y & Schwarzbauer JE (2005) Fibronectin fibrillogenesis, a cell-mediated matrix assembly process. *Matrix Biol* 24(6):389-399.
21. Kubow KE*, et al.* (2015) Mechanical forces regulate the interactions of fibronectin and collagen I in extracellular matrix. *Nat Commun* 6:8026.

bioRxiv preprint doi: https://doi.org/10.1101/232066; this version posted December 10, 2017. The copyright holder for this preprint (which was not certified by peer review) is the author/funder, who has granted bioRxiv a license to display the preprint in perpetuity. It is made available under aCC-BY-NC-ND 4.0 International license.

22. Charras G & Sahai E (2014) Physical influences of the extracellular environment on cell migration. *Nature reviews. Molecular cell biology* 15(12):813.
23. Petrie RJ, Gavara N, Chadwick RS, & Yamada KM (2012) Nonpolarized signaling reveals two distinct modes of 3D cell migration. *J Cell Biol* 197(3):439-455.
24. Poincloux R*, et al.* (2011) Contractility of the cell rear drives invasion of breast tumor cells in 3D Matrigel. *Proceedings of the National Academy of Sciences* 108(5):1943-1948.
25. Sahai E & Marshall CJ (2003) Differing modes of tumour cell invasion have distinct requirements for Rho/ROCK signalling and extracellular proteolysis. *Nature cell biology* 5(8):711.
26. Riching KM*, et al.* (2014) 3D collagen alignment limits protrusions to enhance breast cancer cell persistence. *Biophysical journal* 107(11):2546-2558.
27. Carbonell WS, Ansorge O, Sibson N, & Muschel R (2009) The vascular basement membrane as "soil" in brain metastasis. *PLoS One* 4(6):e5857.
28. Kienast Y*, et al.* (2010) Real-time imaging reveals the single steps of brain metastasis formation. *Nat Med* 16(1):116-122.
29. Farin A*, et al.* (2006) Transplanted glioma cells migrate and proliferate on host brain vasculature: a dynamic analysis. *Glia* 53(8):799-808.
30. Conklin MW*, et al.* (2011) Aligned collagen is a prognostic signature for survival in human breast carcinoma. *The American journal of pathology* 178(3):1221-1232.
31. Scherer HJ (1940) A Critical Review: The Pathology of Cerebral Gliomas. *J Neurol Psychiatry* 3(2):147-177.
32. Stupp R*, et al.* (2005) Radiotherapy plus concomitant and adjuvant temozolomide for glioblastoma. *N Engl J Med* 352(10):987-996.
33. Tamiello C, Buskermolen AB, Baaijens FP, Broers JL, & Bouten CV (2016) Heading in the Right Direction: Understanding Cellular Orientation Responses to Complex Biophysical Environments. *Cellular and molecular bioengineering* 9:12-37.
34. DuFort CC, Paszek MJ, & Weaver VM (2011) Balancing forces: architectural control of mechanotransduction. *Nat Rev Mol Cell Biol* 12(5):308-319.
35. Doyle AD, Wang FW, Matsumoto K, & Yamada KM (2009) One-dimensional topography underlies three-dimensional fibrillar cell migration. *J Cell Biol* 184(4):481-490.
36. Wong S, Guo WH, & Wang YL (2014) Fibroblasts probe substrate rigidity with filopodia extensions before occupying an area. *Proc Natl Acad Sci U S A* 111(48):17176-17181.
37. Paul CD*, et al.* (2016) Interplay of the physical microenvironment, contact guidance, and intracellular signaling in cell decision making. *FASEB journal : official publication of the Federation of American Societies for Experimental Biology* 30(6):2161-2170.
38. Lee P, Lin R, Moon J, & Lee LP (2006) Microfluidic alignment of collagen fibers for in vitro cell culture. *Biomed Microdevices* 8(1):35-41.
39. Tanner K (2012) Regulation of the basement membrane by epithelia generated forces. *Phys Biol* 9(6):065003.
40. Kim J & Tanner K (2016) Three□Dimensional Patterning of the ECM Microenvironment Using Magnetic Nanoparticle Self Assembly. *Current protocols in cell biology*:25.23. 21-25.23. 14.
41. Hsia HC & Schwarzbauer JE (2005) Meet the tenascins: multifunctional and mysterious. *J Biol Chem* 280(29):26641-26644.
42. Mueller MM & Fusenig NE (2011) *Tumor-associated fibroblasts and their matrix* (Springer, Dordrecht ; New York) pp xv, 452 pages.
43. Orend G & Chiquet-Ehrismann R (2006) Tenascin-C induced signaling in cancer. *Cancer Lett* 244(2):143-163.
44. Humphrey JD (2008) Vascular Adaptation and Mechanical Homeostasis at Tissue, Cellular, and Sub-cellular Levels. *Cell Biochemistry and Biophysics* 50(2):53-78.

bioRxiv preprint doi: https://doi.org/10.1101/232066; this version posted December 10, 2017. The copyright holder for this preprint (which was not certified by peer review) is the author/funder, who has granted bioRxiv a license to display the preprint in perpetuity. It is made available under aCC-BY-NC-ND 4.0 International license.

45. Peyton SR & Putnam AJ (2005) Extracellular matrix rigidity governs smooth muscle cell motility in a biphasic fashion. *J Cell Physiol* 204(1):198-209.
46. Kim J & Tanner K (2016) Three-Dimensional Patterning of the ECM Microenvironment Using Magnetic Nanoparticle Self Assembly. *Curr Protoc Cell Biol* 70:25 23 21-25 23 14.
47. Wirtz D (2009) Particle-tracking microrheology of living cells: principles and applications. *Annual review of biophysics* 38:301-326.
48. Staunton JR*, et al.* (2016) Mechanical properties of the tumor stromal microenvironment probed in vitro and ex vivo by in situ-calibrated optical trap-based active microrheology. *Cellular and molecular bioengineering* 9(3):398-417.
49. Ulrich TA, Jain A, Tanner K, MacKay JL, & Kumar S (2010) Probing cellular mechanobiology in three-dimensional culture with collagen-agarose matrices. *Biomaterials* 31(7):1875-1884.
50. Doyle DA (2004) Structural changes during ion channel gating. *Trends Neurosci* 27(6):298-302.
51. Geiger B & Yamada KM (2011) Molecular architecture and function of matrix adhesions. *Cold Spring Harbor perspectives in biology* 3(5).
52. Krammer A, Craig D, Thomas WE, Schulten K, & Vogel V (2002) A structural model for force regulated integrin binding to fibronectin's RGD-synergy site. *Matrix Biology* 21(2):139-147.
53. Lu P, Weaver VM, & Werb Z (2012) The extracellular matrix: A dynamic niche in cancer progression. *The Journal of Cell Biology* 196(4):395-406.
54. Kumar S & Weaver VM (2009) Mechanics, malignancy, and metastasis: The force journey of a tumor cell. *Cancer metastasis reviews* 28(1-2):113-127.
55. Harrison RG (1914) Science and Practise. *Science* 40(1034):571-581.
56. Paul CD, Mistriotis P, & Konstantopoulos K (2017) Cancer cell motility: lessons from migration in confined spaces. *Nature reviews. Cancer* 17(2):131-140.
57. Paul CD, Hung W-C, Wirtz D, & Konstantopoulos K (2016) Engineered Models of Confined Cell Migration. *Annual review of biomedical engineering* 18:159-180.
58. Nuhn JAM, Perez AM, & Schneider IC (2017) Contact Guidance Diversity in Rotationally Aligned Collagen Matrices. *Acta biomaterialia*.
59. Blehm BH, Devine A, Staunton JR, & Tanner K (2016) In vivo tissue has non-linear rheological behavior distinct from 3D biomimetic hydrogels, as determined by AMOTIV microscopy. *Biomaterials* 83:66-78.
60. Staunton JR, Blehm B, Devine A, & Tanner K (2017) In situ calibration of position detection in an optical trap for active microrheology in viscous materials. *Opt. Express* 25(3):1746-1761.
61. Fischer M & Berg-Sørensen K (2007) Calibration of trapping force and response function of optical tweezers in viscoelastic media. *Journal of Optics A: Pure and Applied Optics* 9(8):S239.
62. Neuman KC & Block SM (2004) Optical trapping. *Rev Sci Instrum* 75(9):2787-2809.

bioRxiv preprint doi: https://doi.org/10.1101/232066; this version posted December 10, 2017. The copyright holder for this preprint (which was not certified by peer review) is the author/funder, who has granted bioRxiv a license to display the preprint in perpetuity. It is made available under aCC-BY-NC-ND 4.0 International license.

FIGURES

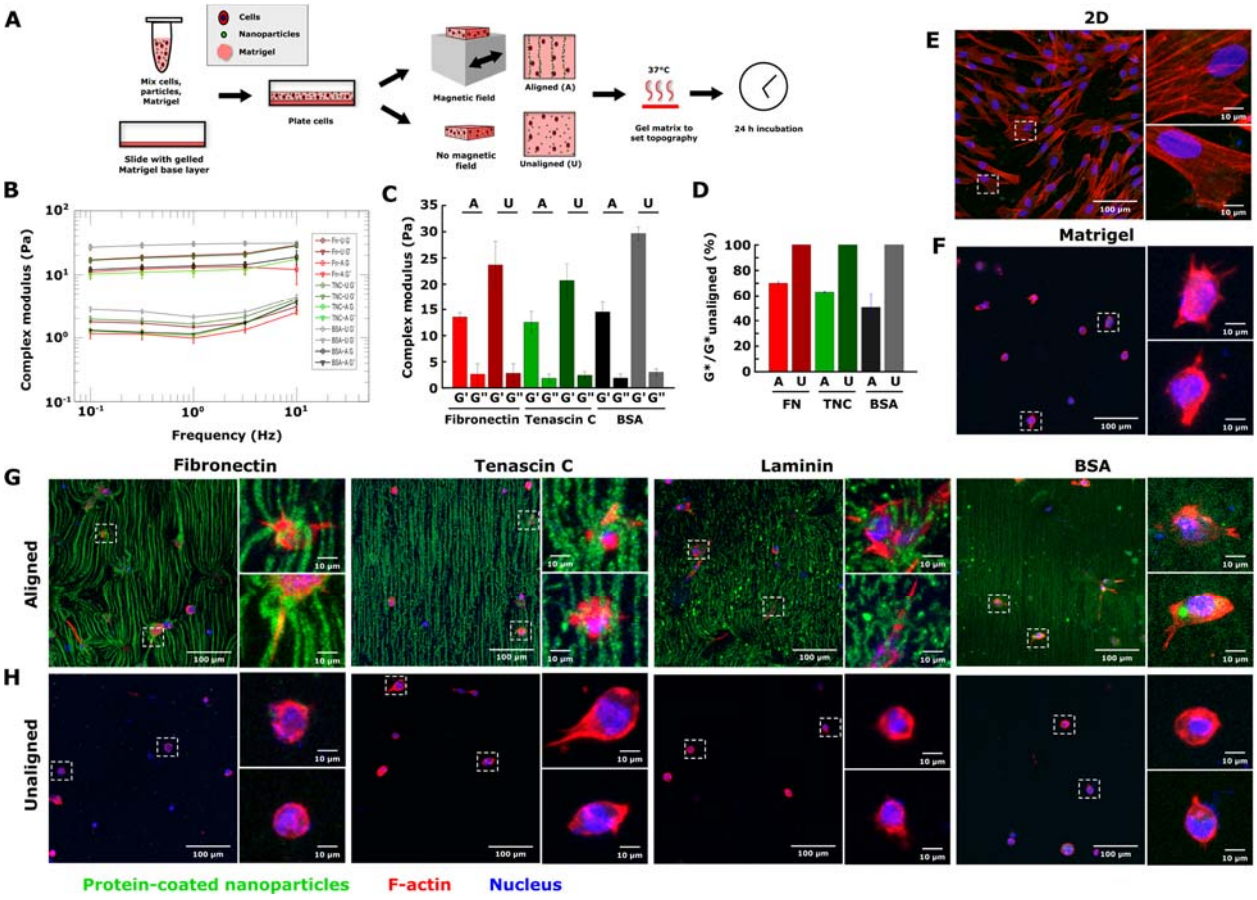

Figure 1. Humanization of the 3D fibrillar matrix system. (A) Schematic of 3D matrix assembly process. Human cells and superparamagnetic nanoparticles were suspended in Matrigel, plated on a glass slide containing a base layer of Matrigel, and either aligned in a magnetic field (aligned gels) or left unaligned and dispersed throughout the matrix (unaligned gels). Gels were then formed by heating at 37°C to set the matrix topography. Cells were fixed for analysis 24 h after seeding. (B) Complex modulus G* (mean ± SEM) vs. frequency curves of aligned and unaligned by parallel small angle oscillatory shear bulk rheology. Elastic (G', circles) and viscous (G'', triangles) components of complex moduli of gels made with nanoparticles coated in human fibronectin (green), tenascin C (red), or BSA (blue), either unaligned (dark green, red, and blue)

bioRxiv preprint doi: https://doi.org/10.1101/232066; this version posted December 10, 2017. The copyright holder for this preprint (which was not certified by peer review) is the author/funder, who has granted bioRxiv a license to display the preprint in perpetuity. It is made available under aCC-BY-NC-ND 4.0 International license.

or aligned (light green, red, and blue) within a Matrigel matrix. Measurements were carried out in duplicate. (C) Bar chart showing the mean ± standard deviation of G' and G'' shown in (B), averaged across frequency. (D) Bar chart showing the complex modulus G* (mean ± standard deviation) in unaligned gels as a percentage of the complex modulus in unaligned gels. The percentage was averaged across all measured frequencies to obtain the mean and standard deviation. (E) Human foreskin fibroblasts (HFF) plated on 2D glass surface coated with Matrigel proteins. (F) HFF cells dispersed in a 3D Matrigel matrix lacking added nanoparticles. (G) Representative images of HFF cells embedded in aligned matrices containing nanoparticles conjugated to fibronectin, tenascin C, laminin, or bovine serum albumin (BSA). (H) Representative images of HFF cells embedded in unaligned matrices containing nanoparticles conjugated to fibronectin, tenascin C, laminin, or bovine serum albumin (BSA). In panels (G, H), nanoparticles are displayed in green. In panels E-H, F-actin is displayed in red and the nucleus in blue. In each panel, overview images are shown, with insets to show detailed cell morphology (cell position in larger image indicated by dashed white boxes). Images are maximum intensity projections of confocal slices containing aligned fibers, or of cells embedded in 3D. Scales are indicated in each image.

bioRxiv preprint doi: https://doi.org/10.1101/232066; this version posted December 10, 2017. The copyright holder for this preprint (which was not certified by peer review) is the author/funder, who has granted bioRxiv a license to display the preprint in perpetuity. It is made available under aCC-BY-NC-ND 4.0 International license.

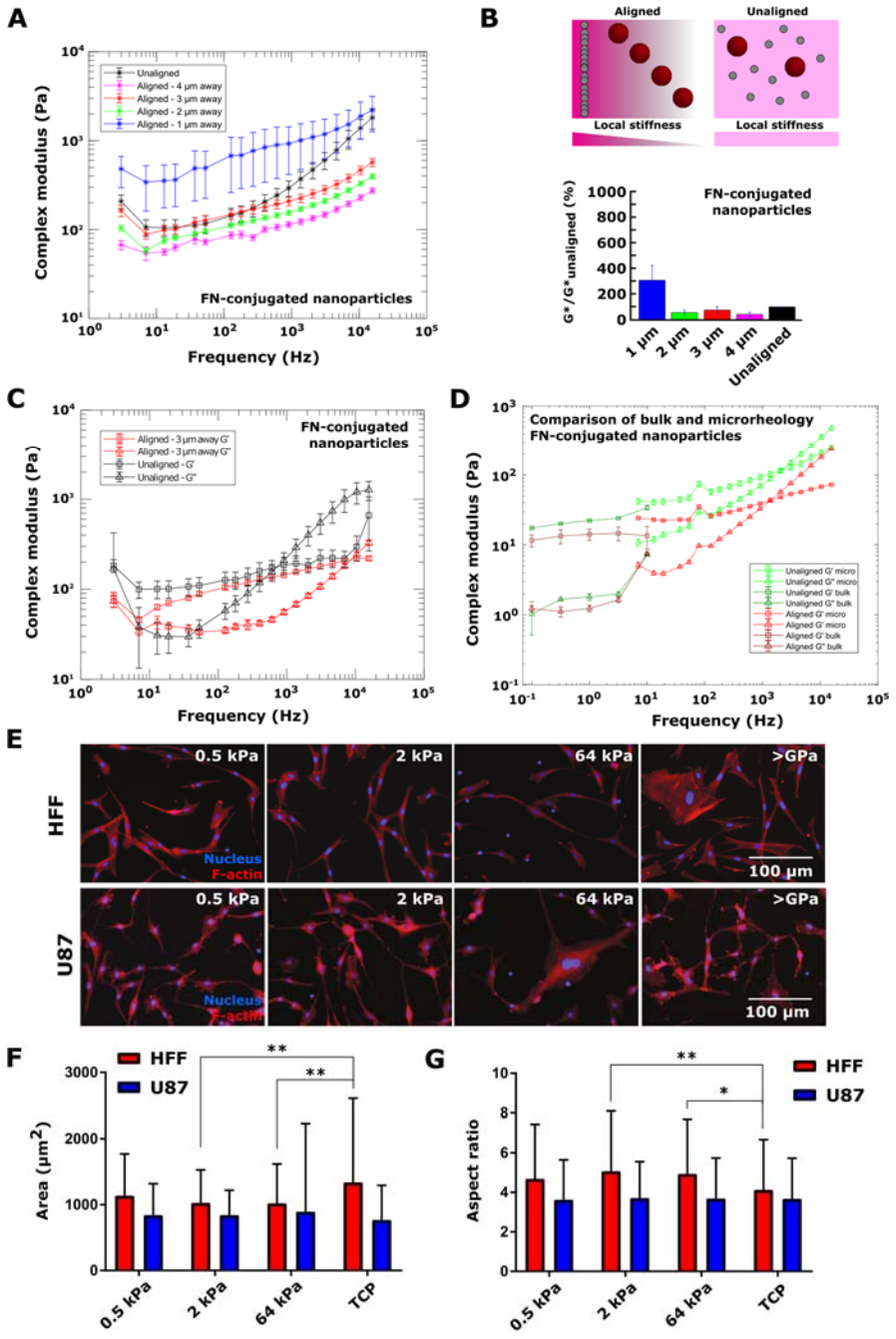

Figure 2. Characterization of the mechanical properties of aligned and unaligned matrices across different length scales. (A) Complex modulus G* (mean ± SEM) vs. frequency curves obtained using optical trap-based microrheology in gels made with nanoparticles conjugated to human fibronectin. Moduli were measured at beads in unaligned gels (black), or in aligned gels at distances of 1 µm (blue), 2 µm (green), 3 µm (red), or 4 µm (pink) away from the nearest fiber.

bioRxiv preprint doi: https://doi.org/10.1101/232066; this version posted December 10, 2017. The copyright holder for this preprint (which was not certified by peer review) is the author/funder, who has granted bioRxiv a license to display the preprint in perpetuity. It is made available under aCC-BY-NC-ND 4.0 International license.

(B) Schematic and summary of microrheology experiments. In aligned gels, local stiffness increased closer to the fibers. In unaligned gels, stiffness was the same throughout the gel. Trend is evident by plotting the complex modulus (mean ± standard deviation), normalized to the complex modulus in unaligned gels, as a function of distance from the nearest fiber. The percentage was averaged across all measured frequencies for a given fiber distance to obtain the mean and standard deviation. (C) Elastic (G', squares) and viscous (G'', triangles) components (mean ± SEM) of complex moduli of gels made with nanoparticles conjugated to human fibronectin. Moduli measured at beads in unaligned gels (black), or in aligned gels at distances of 3 μm away from the nearest fiber (red). (D) Elastic (G', squares) and viscous (G'', triangles) components (mean ± SEM) of complex moduli of gels made with nanoparticles conjugated to human fibronectin. Moduli were measured using either bulk rheology (dark green, dark red) or optical trap-based microrheology (light green, light red). For microrheology measurmenents, the moduli values at all distances from the nearest fiber were combined. Bulk rheology measurements were made in duplicate. For all microrheology measurements, samples were measured in triplicate, with at least 30 beads per sample analyzed. (E) Representative fluorescence images of HFF and U87 cells seeded on silicone substrates with elastic modulus of 0.5, 2, or 64 kPa, or on tissue culture plastic (TCP, >GPa stiffness). Surfaces were coated with 10 μg/ml human fibronectin. F-actin is displayed in red, and the nucleus in blue. Scale is shown. (F) Projected cell area (mean ± standard deviation) and (G) aspect ratio (mean ± standard deviation) as a function of cell type and substrate stiffness. Area and aspect ratio values among conditions were compared using two-way ANOVA with Tukey's multiple comparisons post-test between all combinations of substrate stiffness for a given cell type. *, $p<0.05$; **, $p<0.01$. Measurements were made for two samples

bioRxiv preprint doi: https://doi.org/10.1101/232066; this version posted December 10, 2017. The copyright holder for this preprint (which was not certified by peer review) is the author/funder, who has granted bioRxiv a license to display the preprint in perpetuity. It is made available under aCC-BY-NC-ND 4.0 International license.

per cell type and substrate stiffness, and samples were prepared simultaneously. At least 103 cells were analyzed for each condition.

bioRxiv preprint doi: https://doi.org/10.1101/232066; this version posted December 10, 2017. The copyright holder for this preprint (which was not certified by peer review) is the author/funder, who has granted bioRxiv a license to display the preprint in perpetuity. It is made available under aCC-BY-NC-ND 4.0 International license.

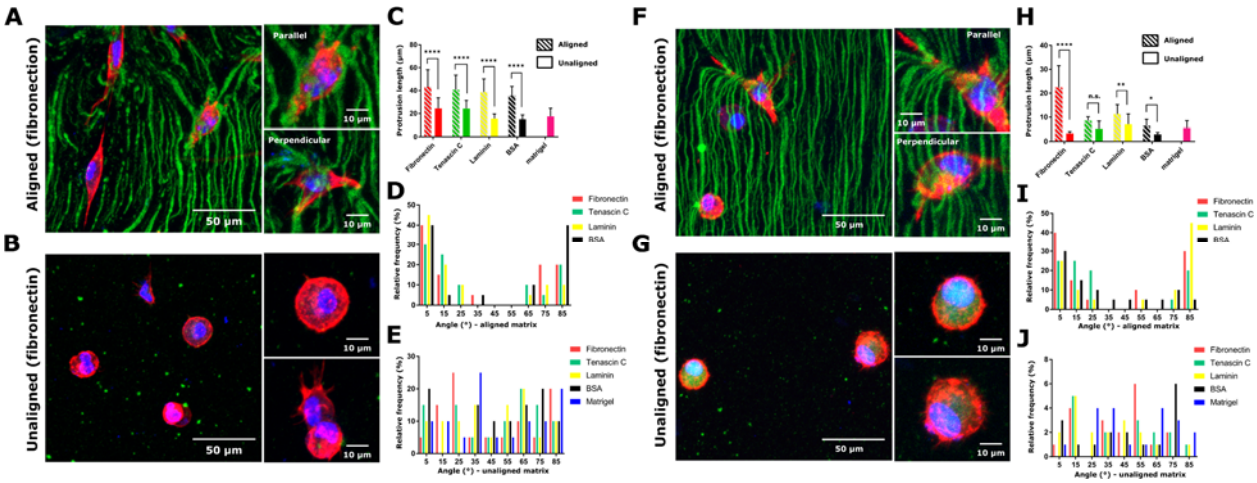

Figure. 3. Increased cell protrusion generation and preferential protrusion orientation in aligned vs. unaligned matrices. (A) Representative image of human foreskin fibroblasts (HFF) embedded in an aligned matrix containing nanoparticles conjugated to fibronectin. Insets show detailed morphology of cells with protrusions extending parallel or perpendicular to fibers. Scales are indicated. (B) Representative image of HFF cells embedded in an unaligned matrix containing nanoparticles conjugated to fibronectin. Insets show detailed morphology of cells. Scales are indicated. (C) Protrusion length (mean ± standard deviation) of HFF cells as a function of matrix alignment status and nanoparticle ECM protein conjugation. Average protrusion length in Matrigel lacking nanoparticles is also shown. ****, $p<0.0001$ by Sidak's multiple comparisons test following two-way ANOVA. (D) Relative frequency distribution of the angle between HFF protrusions and nearest neighbor fibers for matrices containing nanoparticles conjugated to human fibronectin, tenascin C, laminin, or BSA. (E) Relative frequency distribution of the angles between HFF cells in unaligned matrices and the vertical for matrices containing nanoparticles conjugated to human fibronectin, tenascin C, laminin, or BSA. Protrusion direction distribution in Matrigel lacking nanoparticles is also shown. (F) Representative image of U87 cells embedded in an aligned matrix containing nanoparticles conjugated to fibronectin. Insets show detailed morphology of

bioRxiv preprint doi: https://doi.org/10.1101/232066; this version posted December 10, 2017. The copyright holder for this preprint (which was not certified by peer review) is the author/funder, who has granted bioRxiv a license to display the preprint in perpetuity. It is made available under aCC-BY-NC-ND 4.0 International license.

cells with protrusions extending parallel or perpendicular to fibers. Scales are indicated. (B) Representative image of U87 cells embedded in an unaligned matrix containing nanoparticles conjugated to fibronectin. Insets show detailed morphology of cells. Scales are indicated. (C) Protrusion length (mean ± standard deviation) of U87 cells as a function of matrix alignment status and nanoparticle ECM protein conjugation. Average protrusion length in Matrigel lacking nanoparticles is also shown. *, $p<0.05$; **, $p<0.01$; and ****, $p<0.0001$ by Sidak's multiple comparisons test following two-way ANOVA. (D) Relative frequency distribution of the angle between U87 protrusions and nearest neighbor fibers for matrices containing nanoparticles conjugated to human fibronectin, tenascin C, laminin, or BSA. (E) Relative frequency distribution of the angles between U87 cells in unaligned matrices and the vertical for matrices containing nanoparticles conjugated to human fibronectin, tenascin C, laminin, or BSA. Protrusion direction distribution in Matrigel lacking nanoparticles is also shown. In panels (A-B, F-G), nanoparticles are displayed in green, F-actin in red, and the nucleus in blue. Images are maximum intensity projections of confocal slices containing aligned fibers, or of cells embedded in 3D. For each cell type, matrix alignment status, and nanoparticle ECM protein, 20 protrusions were measured from a single 3D matrix.